What Produces Dust Polarization in the HH 212 Protostellar Disk at 878 μm: Dust Self-scattering or Dichroic Extinction?

Chin-Fei Lee[1,2] , Zhi-Yun Li[3], Haifeng Yang[4] , Zhe-Yu Daniel Lin[3], Tao-Chung Ching[5,6] , and Shih-Ping Lai[1,7]

[1] Academia Sinica Institute of Astronomy and Astrophysics, P.O. Box 23-141, Taipei 106, Taiwan; cflee@asiaa.sinica.edu.tw
[2] Graduate Institute of Astronomy and Astrophysics, National Taiwan University, No. 1, Sec. 4, Roosevelt Road, Taipei 10617, Taiwan
[3] Astronomy Department, University of Virginia, Charlottesville, VA 22904, USA
[4] Institute for Advanced Study, Tsinghua University, Beijing, 100084, People's Republic of China
[5] CAS Key Laboratory of FAST, National Astronomical Observatories, Chinese Academy of Sciences, People's Republic of China
[6] National Astronomical Observatories, Chinese Academy of Sciences, A20 Datun Road, Chaoyang District, Beijing 100012, People's Republic of China
[7] Institute of Astronomy and Department of Physics, National Tsing Hua University, Hsinchu, Taiwan

Abstract

We report the results of new dust polarization of a nearly edge-on disk in the HH 212 protostellar system, obtained with the Atacama Large Millimeter/submillimeter Array at $\sim$0.035″ (14 au) resolution in a continuum at $\lambda \sim 878$ μm. Dust polarization is detected within $\sim$44 au of the central source, where a rotationally supported disk has formed. The polarized emission forms V-shaped structures opening to the east, and probably to the west, arising from the disk surfaces and arm structures further away in the east and west, which could be due to potential spiral arms excited in the outer disk. The orientations of the polarization are mainly parallel to the minor axis of the disk, with some in the western part tilting slightly away from the minor axis to form a concave shape with respect to the center. This tilting of the orientations of the polarization is expected from dust self-scattering, e.g., by $50-75$ μm grains in a young disk. The intensity and degree of the polarization both peak near the central source with a small dip at the central source and decrease toward the edges. These decreases in the intensity and degree of polarization are expected from dichroic extinction by grains aligned by poloidal fields, but may also be consistent with dust self-scattering if the grain size decreases toward the edges. It is possible that both mechanisms are needed to produce the observed dust polarization, suggesting the presence of both grain growth and poloidal fields in the disk.

1. Introduction

HH 212 is a young accreting protostellar system with a highly collimated spinning jet (Zinnecker et al. 1998; Lee et al. 2017a) in the Class 0 phase in Orion at a distance of $\sim$400 pc. With a nearly edge-on and vertically resolved disk (Lee et al. 2017b) deeply embedded in a dense rotating molecular core (Wiseman et al. 2001) and an infalling-rotating flattened envelope (Lee et al. 2006, 2014), the disk formation and accretion process in the earliest phase of star formation has become a textbook case to study. The disk is rotationally supported, surrounding a protostar with a mass of $\sim$0.25 $M_\odot$ (Codella et al. 2014; Lee et al. 2017c). Dust polarization has been detected in the disk in submillimeter wavelength at $\sim$875 μm (Lee et al. 2018a), and it can be due to either dichroic extinction by grains aligned magnetically by poloidal fields or dust self-scattering by grains with a maximum size of up to 100 μm in the outer disk. Both possibilities have important implications. If it is the former, then it means poloidal fields have been dragged into the outer disk and can play a role in both the evolution of the disk and the launching of the disk wind(Konigl & Pudritz 2000). If it is the latter, then it means the grains have grown from $\sim$0.1 μm in the interstellar medium (ISM) to 100 μm in the outer disk, and this grain growth can facilitate an earlier start of planet formation in the earliest phase of star formation. Since the dust disk appears to be geometrically thick, the grain settling is not significant, possibly because of turbulence produced by an active accretion. Recent multiwavelength continuum observations have shown

that the disk is likely subject to gravitational instability (Tobin et al. 2020), supporting that the disk is in an active accretion phase.

Recently, dust polarization due to aligned grains has also been detected on larger scales in the dense molecular core and the flattened envelope around the disk, revealing magnetic field morphology there (Galametz et al. 2020; Yen et al. 2021), and thus allowing us to check the possible presence of poloidal fields in the outer disk. In the molecular core at a size scale of $\sim$0.1 pc, the magnetic fields are found to be poloidal with a mean axis at a position angle of $\sim$35° $\pm$ 10°, slightly misaligned with the disk axis (of symmetry) by $\sim$12° counterclockwise (see Figure 11 in Yen et al. 2021). Note that the disk axis has a position angle of $\sim$23°, well aligned with the jet axis (Lee et al. 2017b). In the flattened envelope at a size scale of $\sim$1500 au, the magnetic fields are found to have a similar mean axis to that in the molecular core (Galametz et al. 2020). Interestingly, the innermost flattened envelope with a size scale of $\sim$500 au detected in dust continuum also has an axis with a similar position angle of $\sim$36° $\pm$ 10° (see Figure 1(c) Lee et al. 2017b). This supports the notion that magnetic fields play an important role in the process of the collapse of the molecular core and that the flattened envelope is a pseudo-disk formed by a magnetically guided collapse (Hirano & Machida 2019). Similar pseudo-disks have also been detected in HH 211 (Lee et al. 2019) and OMC-3/MMS6 (Liu 2020). In this scenario, the poloidal fields are dragged into the flattened envelope from the molecular core. These poloidal fields can then be dragged into the outer

disk. Recent detection of disk wind from the outer disk (Tabone et al. 2017, 2020; Lee et al. 2018b, 2021) also suggests the need for poloidal fields there.

The contribution of dust self-scattering to the continuum emission of this disk has also been briefly investigated recently. By modeling the maps of the continuum emission in three wavelengths (from 0.852–3 mm) simultaneously, Lin et al. (2021) found that a pure thermal dust emission can roughly reproduce the dust continuum in those wavelengths. This suggests that the dust self-scattering, even if present at a submillimeter wavelength, could be relatively small in this disk. Similar conclusion were obtained in Galván-Madrid et al. (2018). Considering a maximum grain size of 60–150 μm estimated from scattering-induced polarization in Class I and II protostellar systems in the more evolved phases (Kataoka et al. 2016; Yang et al. 2016b; Bacciotti et al. 2018; Hull et al. 2018), it is also reasonable to consider a maximum grain size smaller than 100 μm in HH 212 in the Class 0 phase.

In this paper, we present our detection of dust polarization in the HH 212 disk in continuum, obtained with the Atacama Large Millimeter/submillimeter Array (ALMA) at three times higher resolution than previous observations, in order to further determine the contributions of dichroic extinction and dust self-scattering. By modeling the morphology of the polarization, the intensity of the polarization, and the degree of the polarization, we find that neither mechanisms can fully reproduce the observations individually and that both mechanisms might be required. Being edge-on and vertically resolved, the HH 212 disk provides the best view to search for poloidal fields and to study the grain growth and settling that are the crucial first steps toward planet formation.

2. Observations

Observations of linear dust polarization of the HH 212 disk were obtained with ALMA in Band 7 in Cycle 5 (Project ID: 2017.1.00044.S). Three observations were taken on 2017 November 27, with a total time of ~98 minutes on the target. A single pointing was used to map the disk with a primary beam of ~17.47 antennas used in the observations, with projected baselines of ~60−8500 m. The maximum recoverable size scale was ~0.4″, enough to map the disk without any significant missing flux. The correlator was set up to have four spectral windows (centered at 334.7, 336.5, 346.6, and 348.4 GHz, respectively), with a total bandwidth of ~8 GHz centered at ~341.5 GHz (or 878 μm correspondingly).

The Common Astronomy Software Applications package was used to calibrate the uv data manually by the ALMA QA2 team, with quasar J5010+1800 as a passband and flux calibrator, quasar J0541−0211 as a gain calibrator, and quasar J0522−3627 as a polarization calibrator. We adopted a super-uniform weighting with a robust factor of 0.5 (with npixels = 0) for the uv data to generate a map of the continuum of the disk at ~341.5 GHz with a synthesized beam (resolution) of ~0.036″ × 0.032″. We also performed a phase-only self-calibration using a map of the intensity of the continuum (Stokes I) to improve the fidelity of the map. In the Stokes I map, the noise level is $\sigma \sim 25\ \mu$Jy beam^{-1} (or 0.233 K). In Stokes Q and U maps, the noise level is $\sigma_p \sim 19\ \mu$Jy beam^{-1} (or 0.177 K). From the Stokes parameters, we can derive the intensity of the linear polarization, fraction of the polarization, and orientation of the polarization. The intensity of the linear polarization is defined as $P_i = \sqrt{Q^2 + U^2 - \sigma_p^2}$ and thus is bias-

corrected. Then the fraction of the polarization is defined as $P = P_i/I$. According to the ALMA Technical Handbook, in Cycle 5 the instrumental error on P is expected to be $\lesssim 0.2\%$ for the disk, which has a size much smaller than $1/3$ of the primary beam. The orientations of the polarization are defined by the E vectors.

3. Results

Throughout this paper, in order to facilitate our presentations, we rotate our maps by 23° clockwise to align the major axis of the disk in the horizontal direction. Figure 1 shows the maps of our polarization observations toward the disk in the continuum at $\lambda \sim 878\ \mu$m. As seen before at $\lambda \sim 852\ \mu$m in Lee et al. (2017b), the the map of the intensity of the continuum shows a "hamburger"-like emission structure for the disk, with a dark lane along the equatorial plane sandwiched by two brighter features arising from the upper and lower disk surfaces. As discussed in that paper, the brighter feature above is slightly brighter than the one below because the nearside of the disk is tilted slightly to the south. In addition, the emission is mainly from the outer edge of the disk on the nearside because of the nearly edge-on orientation, large geometric thickness, and high optical depth of the disk.

Polarized emission has been detected before at a similar wavelength (Lee et al. 2018a). Now at three times higher resolution, we can clearly see that the polarized emission is mainly detected in the dark lane within the centrifugal barrier, which has a radius of ~0.11″ (44 au), where a rotationally supported disk has formed (Lee et al. 2017c). Interestingly, the intensity of polarization shows two peaks in the midplane near the central source on either side at a distance of ~0.02 (8 au), with a small dip at the central source (see also Figure 2). The western peak (right) is brighter than the eastern peak. In addition, the polarized emission extending to the east also peaks near the two (upper and lower) disk surfaces, forming a V-shaped structure near the central source (delineated by the white dotted curve in Figure 1(b)) opening to the east, and then an arm structure further in the east near the midplane. The polarized emission extending to the west could also form such a V-shaped structure near the central source opening to the west, but observations at higher resolution are needed to resolve and confirm it. Nonetheless, it also shows an arm structure further in the west in the midplane. Since the disk is subject to gravitational instability (Tobin et al. 2020) and thus might have spiral arms as seen in the HH 111 disk (Lee et al. 2020), the polarization emission near and in the midplane could be affected by them, forming polarized arm structures there.

The orientations of the polarization (as indicated by the line segments) are rather uniform and mostly parallel to the minor axis of the disk, which is the axis perpendicular to the disk midplane. Going away from the midplane to the disk surfaces, the orientations of the polarization in the west are tilted slightly away from the minor axis to form a concave shape with respect to the center. The degree of the polarization peaks at ~3%–4% near the center at the two peaks of the intensity of the polarization and decreases outwards along the major and minor axes to ~1.5% at the edges and surfaces of the disk (see also Figure 2). The intensity of the polarization further out drops below the 3σ sensitivity, as shown in Figure 2.

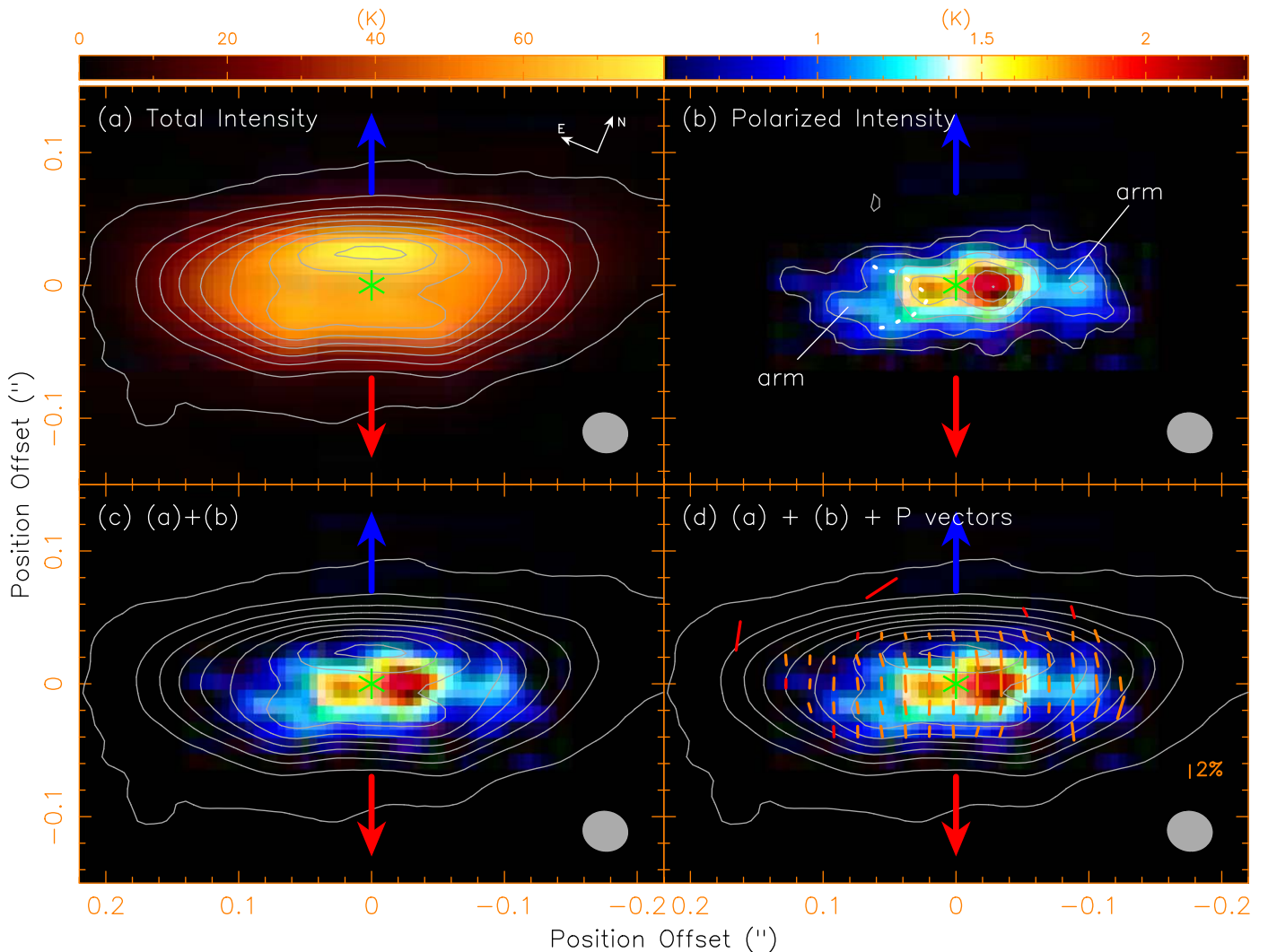**Figure 1.** Observations of polarization toward the HH 212 disk in continuum at $\lambda \sim 878$ μm at $\sim 0.036'' \times 0.032''$ resolution. The blue and red arrows show the approaching and receding sides of the jet axis, respectively. The asterisk marks the possible position of the central source, which is assumed to have coordinates of $5^h43^m51.4086^\circ$ and $-1°2'53''154$, after comparing the maps of the total intensity of the emission between the observations and the models discussed in the text. (a) Map of the total intensity of the emission. Contours start at 10σ with a step of 40σ, where $\sigma = 0.256$ K. (b) Map of the intensity of the polarization. Contours start at $3\sigma_p$ with a step of $2\sigma_p$, where $\sigma_P = 0.173$ K. (c) Map of the total intensity of the emission (contours) and the intensity of the polarization (color). (d) Map of the total intensity of the emission (contours), intensity of the polarization (color), and orientations of the polarization (line segments, red for detections of $(2.5–3)\sigma_p$ and cyan for detections greater than $3\sigma_p$).

4. Polarization Models

In our previous study of dust polarization of this disk at a similar wavelength at a lower resolution of $\sim 0.12''$ (Lee et al. 2018a), the morphology of the polarized emission was not resolved and the polarization could be due to either dichroic extinction by dust grains aligned by poloidal magnetic fields or dust self-scattering by large grains with a size as large as 100 μm. Following up on that, we first introduce a simple parameterized disk model and then explore these two possible mechanisms in more details.

4.1. A Flared Dusty Disk Model

Similar flared disk models have been used to produce the thermal dust emission in this disk (Lee et al. 2017b; Galván-Madrid et al. 2018; Lin et al. 2021). Here, we adopt a similar model to reproduce the observed dust polarization. The disk is composed of dust and gas in vertical hydrostatic equilibrium with a scale height of h_s. In a cylindrical coordinate system, the disk is

assumed to have the following dust mass density and temperature:

$$\rho(R, z) = \rho_t \left(\frac{R}{R_t}\right)^{-p} \exp\left(-\frac{z^2}{2h_s^2}\right)$$

$$T(R, z) = T_t \left(\frac{R}{R_t}\right)^{-q} \exp\left(\frac{z^2}{2h_s^2}\right) \quad (1)$$

where R_t is a reference radius to be defined below, ρ_t and T_t are the dust mass density and temperature in the disk midplane at R_t, respectively, and p and q are the power-law indexes. As in Lee et al. (2017b), we assume that $p = 2$ and $q = 0.75$. Assuming a gas-to-dust mass ratio of 100 and a gas composed of molecular hydrogen and atomic helium, we have the number density of molecular hydrogen at R_t given by

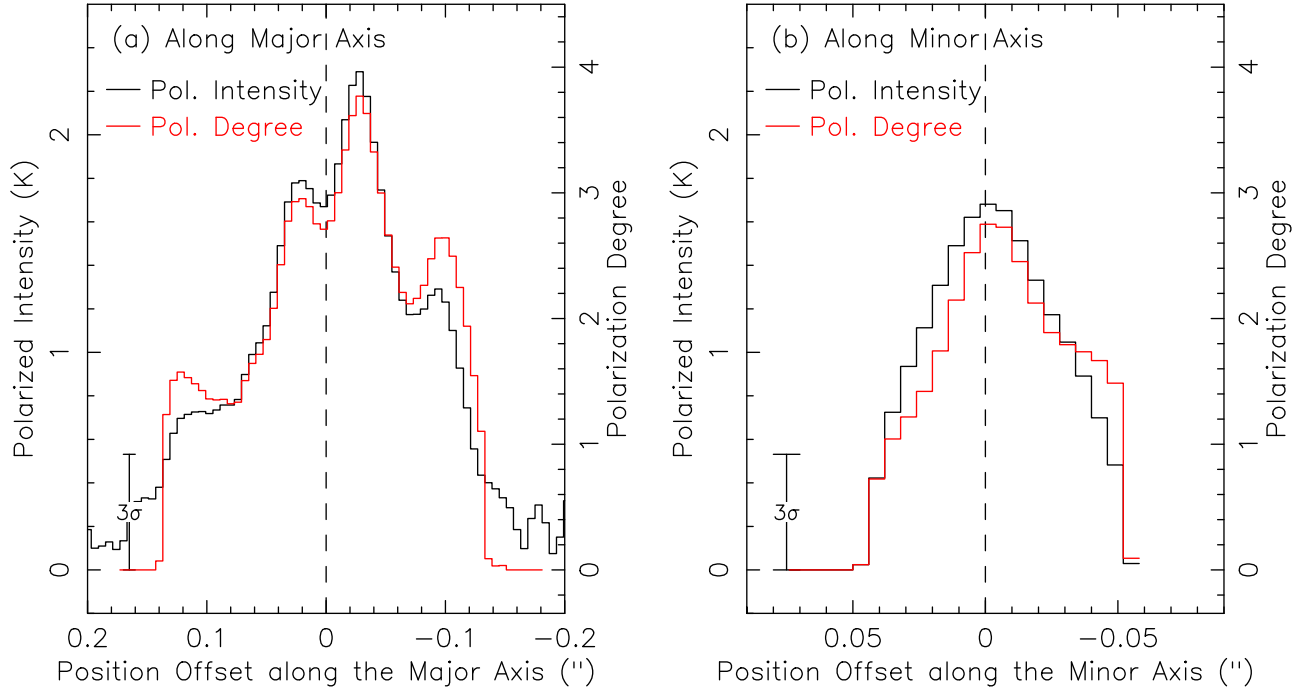$$n_t = \frac{100\,\rho_t}{1.4\,m_{H_2}}. \quad (2)$$

Figure 2. Intensity of the polarization (red curves) and degree of the polarization (black curves) at different position offsets from the central protostar along the (a) major and (b) minor axes.

Here, the number density of helium is assumed to be 0.2 times that of molecular hydrogen.

The scale height is assumed to be proportional to $\frac{c_s}{v_\phi}R$, where c_s is the isothermal sound speed proportional to $T^{1/2}$ and thus to $R^{-q/2}$, and v_ϕ is the rotational velocity assumed to be Keplerian and thus proportional to $R^{-1/2}$ (Lee et al. 2017c). As a result, the scale height is given by

$$h_s(R) = h_t \left(\frac{R}{R_t}\right)^{1+(1-q)/2} \tag{3}$$

with h_t being the scale height at R_t. The total height of the disk can reach $\sqrt{2}\,h_s$. However, as discussed in Lee et al. (2017b), since the continuum emission of the disk becomes geometrically thinner near the outer edge, the total height of the disk is revised to

$$h_o(R) = \sqrt{2}\,h_s \begin{cases} 1 & \text{if } R < R_t, \\ \exp\left[-\left(\frac{R-R_t}{R_o-R_t}\right)^2\right] & \text{if } R_t \leqslant R \leqslant R_o \end{cases} \tag{4}$$

where R_o is the outer radius of the disk and R_t is the radius beyond which the total height of the disk is tapered to roughly match the observed height in the outer edge. Then the disk has a surface density of dust given by

$$\Sigma(R) = \int_{-h_o}^{h_o} \rho\, dz. \tag{5}$$

Radiative transfer assuming LTE is used to calculate the dust emission from the model, using our radiative transfer code in Lee et al. (2017b). A major uncertainty in the model is the dust absorption opacity. Recently, multiwavelength observations in longer wavelengths have been used to constrain it. Using the dust continuum emission at 0.87 and 9 mm at ∼0.1″ resolution, Tobin et al. (2020) found that the disk has Toomre Q values of

1–2.5. By modeling the maps of the continuum emission in three wavelengths (from 0.852–3 mm, including a wavelength similar to the observations here) simultaneously at higher resolution assuming pure thermal dust emission, Lin et al. (2021) estimated the absorption opacity to be $\kappa_{abs} \sim 1.9Q$ cm² g⁻¹ of dust at the wavelength of ∼852 μm. Thus here in our model, adopting $Q \sim 1$, we assume $\kappa_{abs} \sim 1.9$ cm² g⁻¹ of dust at the observed wavelength of 878 μm. Dust self-scattering opacity will be added later when we study the contribution of dust self-scattering to the dust polarization.

The disk is assumed to be nearly edge-on with an inclination of ∼87° (Lee et al. 2021) and the nearside tilted slightly to the south. By matching the observed structure of the continuum emission assuming pure dust thermal emission, we find that $R_t \sim 34 \pm 5$ au (or $0.085'' \pm 0.013''$), $R_o \sim 68 \pm 10$ au (or $0.17'' \pm 0.03''$), $h_s \sim 12 \pm 2$ au (or $0.03'' \pm 0.005''$), $\rho_t \sim 3.0 \pm 0.4 \times 10^{-15}$ g cm⁻³ (or $n_t \sim 6.5 \pm 1.0 \times 10^{10}$ cm⁻³), and $T_t \sim 65 \pm 10$ K, consistent with those found in Lee et al. (2017b), but with a factor of 3 higher n_t due to a factor of 3 lower absorption opacity. Thus, the disk has a total (gas plus dust) mass of ∼$0.14 \pm 0.02\,M_\odot$, which is also about a factor of 3 higher than that derived in Lee et al. (2017b) and thus becomes ∼56% of the protostellar mass. This mass is also consistent with that found by Galván-Madrid et al. (2018), who assumed a similar absorption opacity at 878 μm according to the opacity law they adopted. This disk is so massive and is thus subject to gravitational instability, as discussed in Tobin et al. (2020).

4.2. Dichroic Extinction by Magnetically Aligned Grains

Dichroic extinction is the differential attenuation of two orthogonal components of the E vector of light by magnetically aligned grains (Wood 1997), resulting in a net polarization of light. In this scenario, we assume that the disk is threaded with uniform (vertical) poloidal magnetic fields and the dust grains are aligned by the magnetic fields, with their long axis

perpendicular to the field direction (Andersson et al. 2015). Because the bulk of the disk is optically thick at our observing wavelength and the temperature increases along the line of sight (LOS) into the disk, dichroic extinction (rather than direct emission) by aligned grains is expected to determine the degree and orientation of the polarization relative to the direction of the magnetic field (see, e.g., Figure 1 in Lin et al. 2020, for an illustration).

Our radiative transfer code can be expanded to calculate the maps of the polarization. With an assumption of LTE, the radiative transfer in the Stokes I, Q, and U parameters can be given by the following (see also POLARIS in Reissl et al. 2016):

$$\frac{d}{\rho ds}\begin{pmatrix} I \\ Q \\ U \end{pmatrix} = -\begin{pmatrix} C_{\mathrm{ext}} & C_{\mathrm{pol}}\cos 2\psi & C_{\mathrm{pol}}\sin 2\psi \\ C_{\mathrm{pol}}\cos 2\psi & C_{\mathrm{ext}} & 0 \\ C_{\mathrm{pol}}\sin 2\psi & 0 & C_{\mathrm{ext}} \end{pmatrix}\begin{pmatrix} I \\ Q \\ U \end{pmatrix}$$
$$+ B_\nu(T)\begin{pmatrix} C_{\mathrm{ext}} \\ C_{\mathrm{pol}}\cos 2\psi \\ C_{\mathrm{pol}}\sin 2\psi \end{pmatrix}.$$

(6)

The cross section of the extinction per gram (i.e., extinction opacity) and the cross section of the polarization per gram (i.e., polarization opacity) can be given by (see Lee & Draine 1985)

$$C_{\mathrm{ext}} = \kappa_{\mathrm{abs}}\left[1 - \alpha\left(\frac{\cos^2\gamma}{2} - \frac{1}{3}\right)\right]$$
$$C_{\mathrm{pol}} = \alpha\kappa_{\mathrm{abs}}\cos^2\gamma$$

(7)

where γ is the angle between the local $\boldsymbol{B}$ vector and the plane of the sky, and $\psi = \phi + 90°$ is the angle of the polarization measured from the north (ordinate axis) to the east, with ϕ being the angle between the projection of the local $\boldsymbol{B}$ vector on the plane of the sky and north. In order to calculate the quantities of the polarization, we assume a polarization efficiency α, which defines the maximum fraction of polarization in an optically thin region (Fiege & Pudritz 2000; Padoan et al. 2001). After the integration along each LOS, the resulting intensity, fraction, and angle of polarization can then be given, respectively, by

$$P_i = \sqrt{Q^2 + U^2}$$ (8)

$$P = \frac{P_i}{I}$$ (9)

and

$$\psi = \frac{1}{2}\tan^{-1}\frac{U}{Q}.$$ (10)

By matching the fraction of the polarization of ~ 0.03 observed in the optically thick central region of the disk, we find that a value of $\alpha \sim 0.075$ is required in the model. In this case, $C_{\mathrm{ext}} \approx \kappa_{\mathrm{abs}}$.

Figure 3 shows the results of the model. The map of the total intensity of the emission shows a dark lane along the major axis sandwiched by two brighter curved features above and below because the disk midplane is cooler and optically thicker than the surfaces. Since the disk's nearside is tilted slightly to the south, the upper disk surface is slightly exposed and thus becomes brighter

than the lower one. The whole disk is optically thick. In particular, the optical depth peaks at the center with a value greater than 100, and it decreases outward and drops to ~ 1 near the outer edges and outer disk surfaces. The emission in the disk is polarized. Along the major axis, the intensity of the polarization peaks at the center and decreases outward and drops to zero at $\sim 0.11''$ (44 au), where the optical depth drops to $3-5$, and then increases again in the optically thinner outer edges. The initial decrease of the fraction of the polarization with distance is physically reasonable since the fraction of polarization produced by dichroic extinction along high optical depth sight lines is determined mainly by the temperature gradient along the LOS, which is the highest toward the center. As the sight line moves toward the outer edge of the disk, both the optical depth and the LOS temperature gradient decrease, weakening the contribution of the dichroic extinction to the polarization relative to that of the dichroic emission. Going away from the midplane to the disk surfaces, the intensity of the polarization increases with the increasing distance and peaks near the disk surfaces where the temperature is higher, outlining the disk surfaces. Then the intensity of the polarization drops to zero at $\sim 0.03''$ (12 au), where the optical depth drops to $3-5$, and then increases again in the optically thinner outer surfaces. As a result, when the optical depth drops to $3-5$, the intensity of the polarization and the resulting drop in the degree of polarization to zero, form an elliptical gap in the polarization around the inner disk. Interior to the gap in the polarization in the inner optically thicker region, the orientations of the polarization are parallel to the direction of the poloidal field and thus the minor axis because of the dichroic extinction and the temperature gradient, as discussed in Lee et al. (2018a) and Lin et al. (2020). Going across the gap in the polarization to the outer optically thinner region, the orientations of the polarization flip by 90° to be perpendicular to the direction of the poloidal field (and thus the minor axis). In this outer region, direct emission by aligned grains is dominant.

Figure 4 shows the results of the model convolved to the observed beam to be compared with the observations. The map of the total intensity of the emission also shows a dark lane sandwiched by two brighter features, similar to that seen in the observations. The gap in the polarization can still be seen in the convolved map around the inner disk. Interior to the gap in the polarization, the polarized emission from the upper and lower disk surfaces merge and form a single elongated structure of polarization in the dark lane, with hints of V-shaped structures opening to the east and west still discernible, although far less prominent compared to the unconvolved map. This polarization structure, although less clearly V-shaped, could correspond to that observed in the dark lane, which shows a V-shaped structure opening to the east and probably another one opening to the west. Note that we do not intend to reproduce the polarized arm structures, which could be affected by potential spiral arms, as discussed earlier. Both the intensity and degree of the polarization of the beam convolved model peak at the center and decrease outward, also roughly similar to the observed trends. The orientations of the polarization are parallel to the minor axis, and are also similar to the observed orientations, except for those in the west near the disk surfaces where the observed orientations are tilted slightly away from the minor axis to form a concave shape with respect to the center. However, unlike the observations that show two polarized emission peaks near the central source with a small dip in between, only one single polarized emission peak is seen in the model toward the central source.
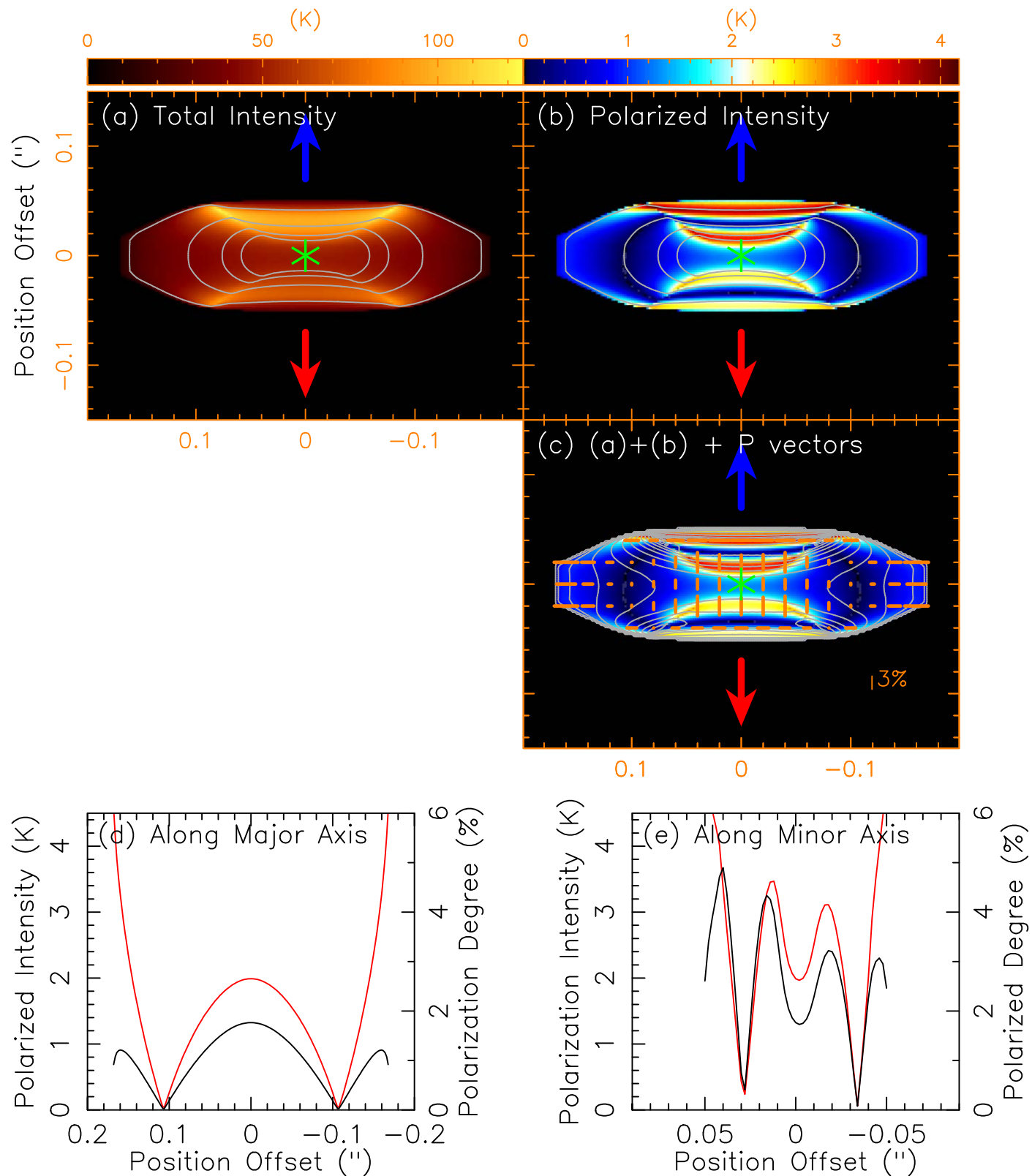
Figure 3. Dichroic extinction model by grains aligned magnetically by poloidal fields. (a) Map of the total intensity of the emission (color) with optical depth (contours). Contours start from 1 with a step of 3. Only the first four contours are plotted. (b) Map of the intensity of the polarization (color) with optical depth (contours). (c) Map of the total intensity of the emission (contours), intensity of the polarization (color), and degrees of polarization (line segments with the length for the degrees). (d) Intensity of the polarization (black curve) and degree of the polarization (red curve) along the major axis of the disk. (e) Intensity of the polarization (black curve) and degree of the polarization (red curve) along the minor axis of the disk.
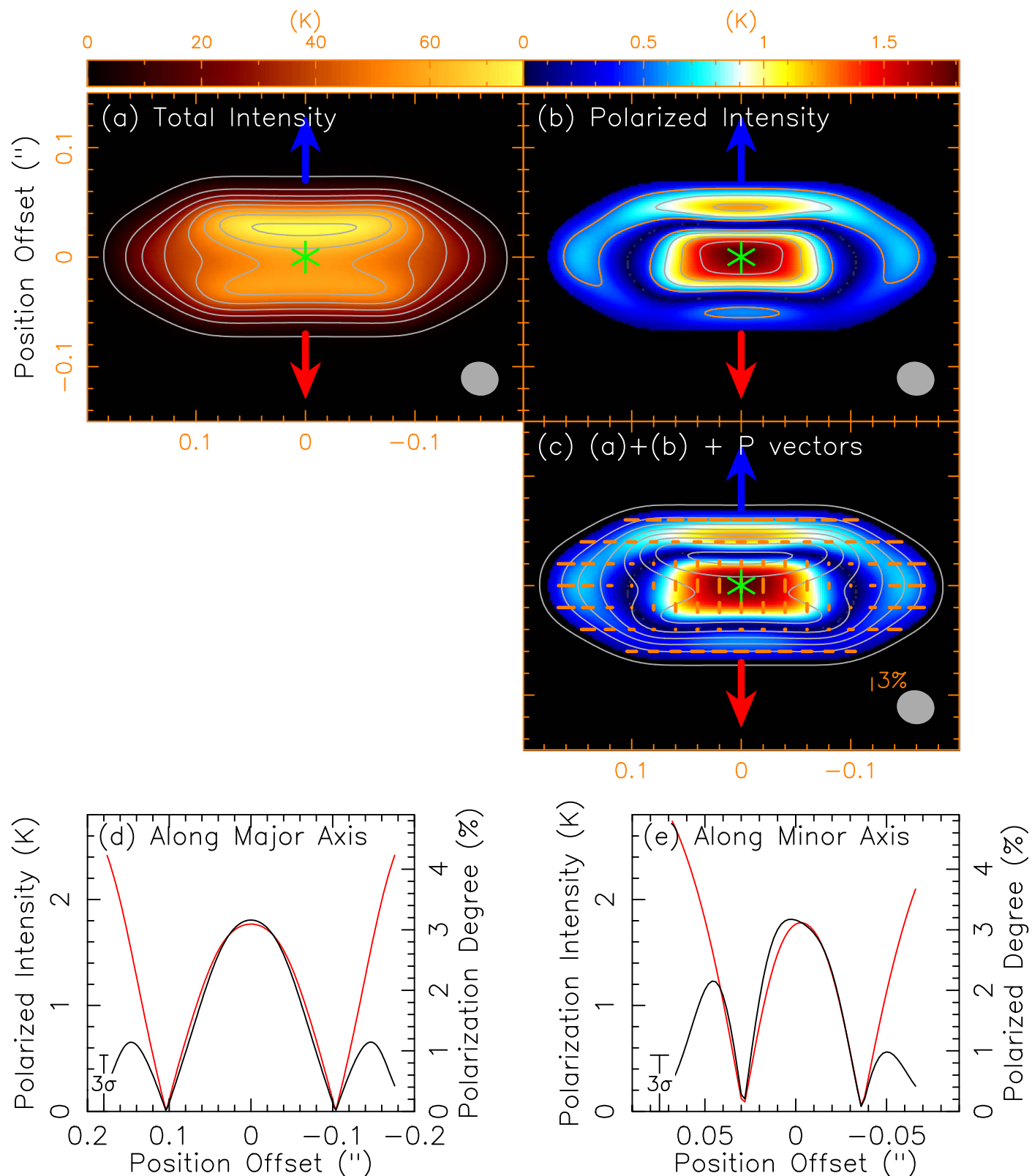
Figure 4. Same as Figure 3 but convolved to the observed beam to be compared with the observations. The contour levels in (a) and (c) are the same as those in Figure 1(a). The contour levels in panel (b) are the same as those in Figure 1(b), with the lowest contour (orange) showing a 3σ sensitivity level in our observations.

In the model, the intensity of the polarization drops to zero in the gap in the polarization and then increases outside. Outside the gap in the polarization, although the polarized emission is much fainter than that inside, the polarized emission in the upper surface and outer disk above the 3σ sensitivity level (encompassed by the orange contour) in Figure 4(b) should still be detectable in the current observations, with a flip of the orientation of the polarization to be perpendicular to the minor

axis. However, such an increase in the intensity of the polarization and a flip of the orientation of the polarization the outer disk are not detected here. Thus, the gap in the polarization and the increase of the intensity of the polarization around the disk predicted in this model might not exist in the observations but deeper observations are needed to check them.

4.3. Dust Self-scattering by Submillimeter-sized Grains

Dust self-scattering by large grains (100 μm or larger) has been found to contribute significantly to the (sub)millimeter dust polarization in the protoplanetary disks in the later phase of star formation (Kataoka et al. 2015, 2016; Yang et al. 2016a, 2016b, 2017), as seen in the evolved disks in, e.g., HL Tau (Kataoka et al. 2017; Stephens et al. 2017), CW Tau and DG Tau (Bacciotti et al. 2018), HD 142527 (Ohashi et al. 2018), IM Lup (Hull et al. 2018), and HD163296 (Dent et al. 2019). It can also contribute to the dust polarization in the early phase in the protostellar disks if the dust grains have grown to 100 μm in size (Alves et al. 2018; Harris et al. 2018; Sadavoy et al. 2018a, 2018b). Since the scattering opacity is still uncertain, we parameterize it by

$$\kappa_{\rm sca} = \frac{\omega}{1 - \omega} \kappa_{\rm abs} \qquad (11)$$

where $\kappa_{\rm abs}$ is the absorption opacity and ω is the albedo defined as

$$\omega = \frac{\kappa_{\rm sca}}{\kappa_{\rm abs} + \kappa_{\rm sca}}. \qquad (12)$$

This albedo can be linked to grain size. For example, with a size distribution of $n(a) \propto a^{-3.5}$ and a mixture of silicate, water ice, and organics, maximum grain sizes of 10, 25, 50, 75, and 100 μm, Kataoka et al. (2015) estimated an albedo of $\sim$0, 0.036, 0.23, 0.50, and 0.70, respectively, at the observed wavelength of 870 μm, although the exact values depend on grain properties (such as shape and composition), which are uncertain.

Since the disk here is young in the deeply embedded, actively accreting protostellar phase, the grain size is expected to be smaller than 100 μm (Galván-Madrid et al. 2018; Lin et al. 2021). Since the morphology of the dust polarization due to dust self-scattering does not depend much on the actual size of the grains (as long as the grains are not too large compared to the observing wavelength) and the grain composition, we adopt an albedo of 0.5, or equivalently assume a scattering opacity the same as the absorption opacity, to study the dust self-scattering effect. For demonstration purposes, we first derive the dust-scattering matrix with the Mie approximation using the optical constants of an amorphous silicate (amorphous pyroxene with 70% magnesium and 30% iron) (Jaeger et al. 1994; Dorschner et al. 1995), a grain size of 100 μm, and a material density of 1.675 g cm^{-3} (Birnstiel et al. 2018), and then scale it down to have a scattering opacity the same as that of the absorption opacity to be consistent with our adopted albedo. Then, we use the RADMC-3D[8] code (Dullemond et al. 2012) to produce maps of the polarization. Since the dust-scattering opacity adds an additional optical depth and thus an attenuation of the dust emission, a higher temperature with $T_t \sim 95 \pm 14$ K, which is about 50% higher than that without

dust scattering, is required to roughly match the observed brightness temperature.

Figure 5 shows the results of the model. Like the dichroic extinction model, the map of the total intensity of the emission also shows a dark lane in the major axis sandwiched by two brighter features arising from the disk surfaces. The dark lane is wider because of a larger optical depth and the emission is scattered away from the midplane. However, unlike the dichroic extinction model, no gap in the polarization is seen. In addition, the intensity of the polarization shows a dip at the center because the radiation is most symmetric about the center. It increases outwards in all directions and peaks near the edges and at the disk surfaces because of the increase in asymmetry and also the increase in temperature for the disk surfaces. It then drops rapidly to zero at the edges and above the surfaces. Like the total intensity of the emission, the intensity of the polarization from the upper disk surface is brighter than that from the lower one. The degree of the polarization also shows a similar trend to the intensity of the polarization, except near the two edges where the degree of the polarization continues to increase toward the edges due to the faster decrease of the total intensity of the emission. The orientations of the polarization are parallel to the minor axis near the midplane and then tilted slightly away from the minor axis to form a concave shape with respect to the center when going away from the midplane to the upper and lower disk surfaces.

Figure 6 shows the results of the model convolved to the observed beam. The map of the total intensity of the emission shows a similar structure to that observed. The orientations of the polarization are mostly parallel to the minor axis, and tilted slightly away from the minor axis to form a concave shape with respect to the center when going away from the midplane to the disk surfaces, similar to that seen in the observations. Unlike the dichroic extinction model, the upper disk and lower disk surfaces in the intensity of the polarization do not merge to form a single elongated structure because the dark lane is wider and the lower disk surface is much fainter. In addition, unlike those seen in the observations, the intensity and degree of the polarization in the model increase toward the edges along the major axis and drop rapidly at the edges. With the intensity of the polarization peaks near the two edges, the resulting dip in the intensity of the polarization is much wider than that observed, inconsistent with the observations. We have tried a smaller albedo of 0.25. In this case, the polarized emissions from the upper disk and lower disk surfaces move slightly closer to the midplane, forming V-shaped structures opening to the east and west, roughly similar to that observed. However, the intensity of the polarization still peaks at the two edges, inconsistent with the observations. Moreover, the intensity of the polarization everywhere becomes lower than the 3σ sensitivity limit in our current observations.

5. Discussion

Dust polarization is detected in the HH 212 disk within the centrifugal barrier at $\sim$44 au, where a rotationally supported disk has formed. The comparison of our simple models with the observations suggests that neither a simple dichroic extinction model by magnetically aligned grains nor a simple dust self-scattering model can fully account for the observed morphology of the polarization, intensity of the polarization, and the degree of the polarization simultaneously. The dichroic extinction model can produce an elongated polarized structure
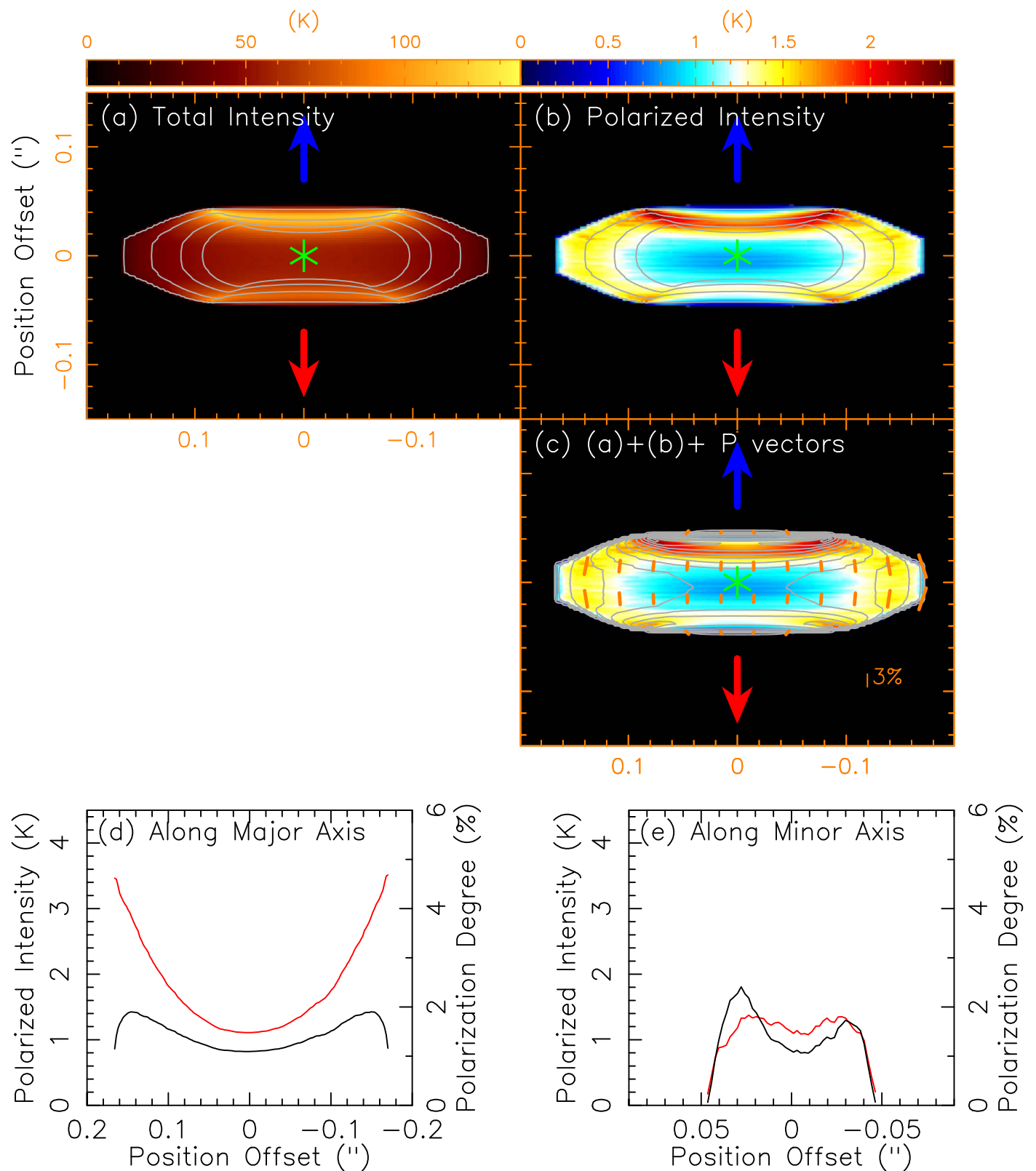

Figure 5. Dust self-scattering model. Same as Figure 3.

in the dark lane, with hints of V-shaped structures opening to the east and west, similar to the observations. It can also produce a decrease in the intensity of the polarization and the degree of the polarization in the dark lane from the center toward the edges. However, it cannot produce a small dip in the intensity of the polarization at the center. In addition, it produces a gap in the polarization and polarized emission with orientations of polarization perpendicular to the minor axis outside the gap in the outer disk, which are not seen in the observations. Also, it cannot produce the observed slight tilt of
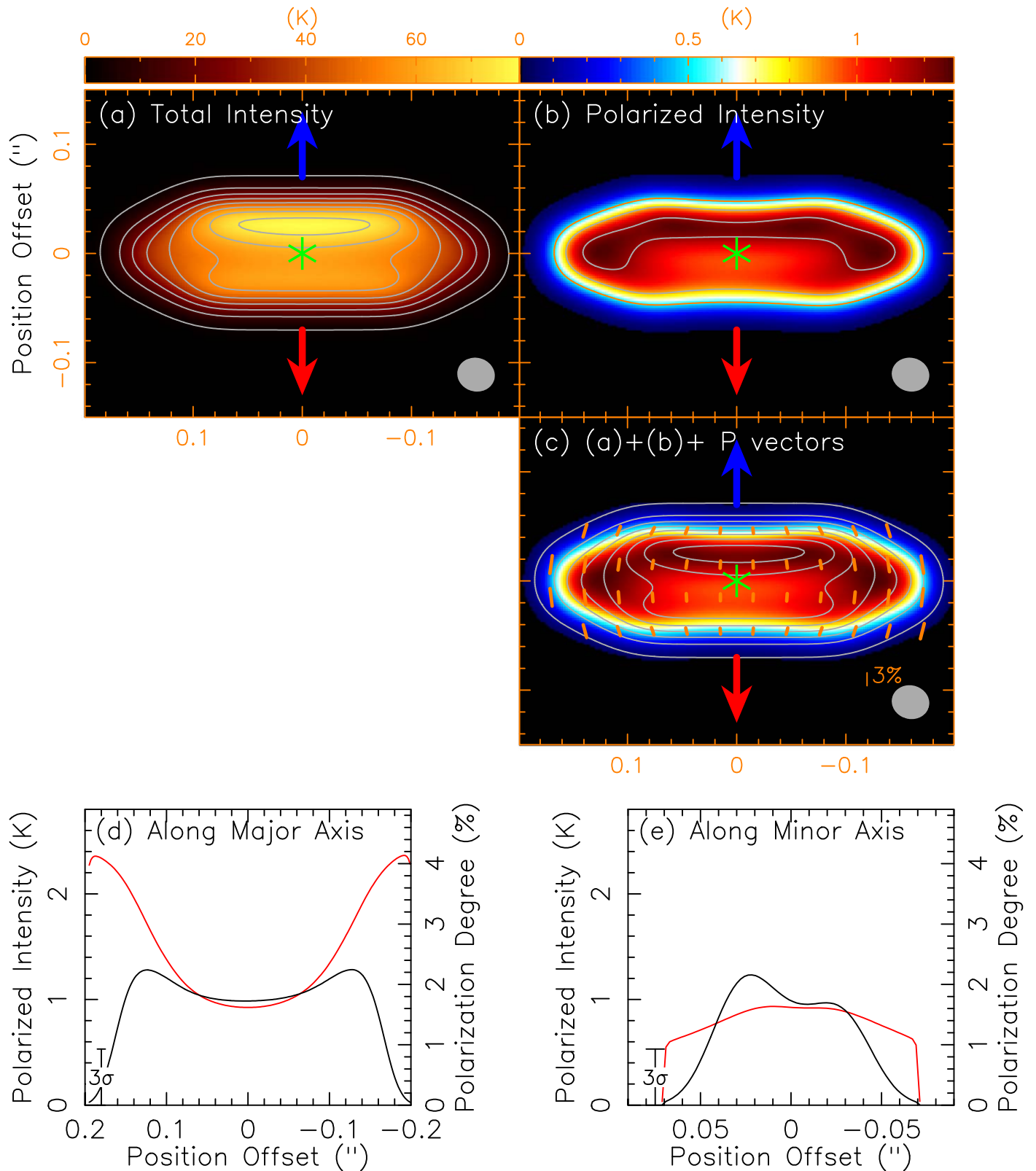
Figure 6. Same as Figure 5 but convolved to the observed beam to be compared with the observations. The contour levels are the same as those in Figure 4.

the orientations of the polarization away from the minor axis in the western part of the disk above and below the disk midplane. On the other hand, the dust self-scattering model can roughly produce the observed orientations of the polarization. However, it cannot produce the observed intensity of the polarization and

the degree of the polarization from the center to the outer edges. Moreover, the intensity of the polarization in the model always peaks near the two edges, producing a dip much wider than that observed. Adding a flattened envelope around the disk may reduce the intensity of the polarization near the edges by

shining radiation into the disk, but may not be sufficient to reduce it down to zero.

None of our two simple models can reproduce the observed small dip in the intensity of the polarization toward the position of the central source. This dip in the intensity of the polarization is unlikely to be a polarization hole due to depolarization of unresolved complicated orientations of polarization, as seen in, e.g., Serpens SMM1 (Hull et al. 2017), because the orientations of polarization there are rather uniform. Our dichroic extinction model assumes a constant polarization efficiency and thus grain alignment efficiency. A decrease of grain alignment efficiency toward the center, as proposed to explain the decrease of the fraction of the polarization toward the region with the higher column density (Galametz et al. 2018), may help to produce a small dip in the intensity of the polarization at the center. However, further work is needed to study this possibility. On the other hand, our self-scattering model assumes a single albedo and thus the same maximum grain size all over the disk. It is possible that the maximum grain size may decrease from the inner to the outer disk across the centrifugal barrier. For example, the grains newly accreted from the envelope to the outer disk may be too small to scatter (sub)millimeter photons efficiently. Further modeling is needed to check if the decrease in maximum grain size toward the edges can produce a small polarized intensity dip at the center and a decrease of polarized intensity toward the edges.

It is also possible that both mechanisms contribute to the dust polarization in the HH 212 disk. The dichroic extinction model better produces the decrease in the intensity of the polarization and the degree of the polarization in the dark lane toward the edges, while the scattering model better produces the tilt of the orientations of the polarization away from the minor axis when going away from the midplane to the disk surfaces. In addition, combining these two models may also produce two polarized intensity peaks near the central source with a small dip in the polarization at the central source, as seen in the observation. Since RADMC-3D cannot treat scattering by aligned (nonspherical) grains at the present time, we will defer the combined modeling to a future publication. As mentioned in the introduction, poloidal fields can be dragged from the dense molecular core into the innermost part of the envelope and then to the outer disk. If this is the case, the magnetic fields may be responsible for launching the rotating SO/SO_2 outflow extending out from the disk (Tabone et al. 2017; Lee et al. 2018b, 2021). Observations at higher resolution are needed to determine the location of the magnetic fields more accurately. Also as mentioned in the introduction, recent multiwavelength observations suggested that the dust self-scattering contribution to the dust continuum emission should be smaller than the thermal dust emission (Lin et al. 2021), otherwise the required temperature in the disk would be too high. As seen in our model with an albedo $\omega = 0.5$, the temperature in the disk is already ~50% higher than that without dust scattering. According to Kataoka et al. (2015), albedos are 0.23, 0.50, and 0.70 for maximum grain sizes of 50, 75, and 100 μm, respectively, which then result in $\kappa_{sca} = 0.23, 1.0,$ and 2.33 κ_{abs}, respectively. Thus, in order to have a scattering opacity comparable to or smaller than the absorption opacity, the grains can have a maximum size of $50-75$ μm, which is reasonable for a Class 0 disk in the outer edges. Moreover, since the disk is vertically extended, the grain settling is unlikely to have taken place significantly. Hence, the

grains are likely relatively small. Furthermore, smaller grains are better for magnetic alignment.

We can estimate whether the midplane temperature inferred from our modeling can be produced by viscous heating due to disk accretion. Since the disk here is optically thick, the midplane temperature due to viscous heating would be (Shakura & Sunyaev 1973)

$$T_{mid}(R) \sim \tau_R^{1/4} T_{eff}(R) \tag{13}$$

where T_{eff} is the effective (surface) temperature of the disk at $\tau \sim 1$ given by

$$T_{eff}(R) \sim \left(\frac{3GM\dot{M}}{8\pi\sigma R^3} \right)^{1/4} \tag{14}$$

and τ_R is the Rosseland mean optical depth defined as

$$\tau_R \equiv \frac{1}{2} \Sigma \kappa_R \tag{15}$$

with σ being the Stefan Boltzmann constant, κ_R being the Rosseland mean opacity per gram of dust, and Σ being the surface density of the dust. In HH 212, with $M \sim 0.25$ $M_\odot$ (Codella et al. 2014; Lee et al. 2014, 2017c) and $\dot{M} \sim 5 \times 10^{-6}$ $M_\odot$ yr^{-1} (Lee et al. 2014), we have $T_{eff} \sim 20$ K at R_t or 34 au. In our model, the dust surface density $\Sigma \sim 1.14$ g cm^{-2} at R_t. For a disk temperature between 20 and 100 K at that radius, the blackbody radiation peaks at wavelength $\lambda_{peak} \sim 29-145$ μm, according to Wien's displacement law. Then, assuming a maximum grain size of 100 μm and judging from Figure 1 in Kataoka et al. (2015) that shows the dust opacity versus wavelength, we have $\kappa_R < 200$ cm^2 g^{-1} and thus $\tau_R < 114$. Thus, the midplane temperature in the disk should be less than 65 K at R_t. Additional heating can come from irradiation by the central stellar object, so the midplane temperature of about 65 K at R_t inferred in our dichroic extinction model appears reasonable. We refrain from a detailed modeling of the temperature structure because it depends on the dust opacities, which are uncertain. Nevertheless, a midplane temperature of ~95 K at R_t as in our dust self-scattering model would require a Rosseland mean opacity of ~5 times higher and is thus too high.

6. Conclusions

We have resolved the dust polarization in the HH 212 disk in continuum at $\lambda \sim 878$ μm and found it to have mainly arisen within the centrifugal barrier at ~44 au, where a rotationally supported disk has formed. The polarized intensity forms V-shaped structures opening to the east and probably the west arising from the disk surfaces and arm structures further away in the east and west. The orientations of the polarization are mainly parallel to the minor axis, with some in the western part tilting slightly away from the minor axis to form a concave shape with respect to the center when going away from the midplane to the upper and lower disk surfaces. The intensity of the polarization and the degree of the polarization both peak near the central source with a small dip at the central source and decrease toward the disk outer edges. The observed tilt in the orientations if the polarization orientations of the polarization away from the minor axis are more consistent with that expected from dust self-scattering by $50-75$ μm grains, but the observed decreases in the intensity of the polarization and the degree of the polarization

from the center to the edges are more consistent with those expected from dichroic extinction by grains aligned by poloidal fields. The decreases in the intensity of the polarization and the degree of the polarization toward the edges may also be consistent with dust self-scattering if the grain size decreases toward the edges, as expected, if the grain size increases across the centrifugal barrier from the outer edges. It is possible that both mechanisms are needed to produce the observed dust polarization, suggesting the presence of both poloidal fields and grain growth in the disk. In addition, the polarized arm structures could be due to potential spiral arms excited in the outer disk as the disk has been found to be gravitationally unstable.

ORCID iDs

Chin-Fei Lee ● https://orcid.org/0000-0002-3024-5864
Haifeng Yang ● https://orcid.org/0000-0002-8537-6669
Tao-Chung Ching ● https://orcid.org/0000-0001-8516-2532
Shih-Ping Lai ● https://orcid.org/0000-0001-5522-486X

References

Alves, F. O., Girart, J. M., Padovani, M., et al. 2018, A&A, 616, A56
Andersson, B.-G., Lazarian, A., & Vaillancourt, J. E. 2015, ARA&A, 53, 501
Bacciotti, F., Girart, J. M., Padovani, M., et al. 2018, ApJL, 865, L12
Birnstiel, T., Dullemond, C. P., Zhu, Z., et al. 2018, ApJL, 869, L45
Codella, C., Cabrit, S., Gueth, F., et al. 2014, A&A, 568, L5
Dent, W. R. F., Pinte, C., Cortes, P. C., et al. 2019, MNRAS, 482, L29
Dorschner, J., Begemann, B., Henning, T., et al. 1995, A&A, 300, 503
Dullemond, C. P., Juhasz, A., Pohl, A., et al. 2012, RADMC-3D: A multi-purpose radiative transfer tool, Astrophysics Source Code Library, ascl:1202.015
Fiege, J. D., & Pudritz, R. E. 2000, ApJ, 544, 830
Galametz, M., Maury, A., Girart, J. M., et al. 2018, A&A, 616, A139
Galametz, M., Maury, A., Girart, J. M., et al. 2020, A&A, 644, A47
Galván-Madrid, R., Liu, H. B., Izquierdo, A. F., et al. 2018, ApJ, 868, 39
Harris, R. J., Cox, E. G., Looney, L. W., et al. 2018, ApJ, 861, 91
Hirano, S., & Machida, M. N. 2019, MNRAS, 485, 4667
Hull, C. L. H., Mocz, P., Burkhart, B., et al. 2017, ApJL, 842, L9
Hull, C. L. H., Yang, H., Li, Z.-Y., et al. 2018, ApJ, 860, 82
Jaeger, C., Mutschke, H., Begemann, B., et al. 1994, A&A, 292, 641
Kataoka, A., Muto, T., Momose, M., et al. 2015, ApJ, 809, 78
Kataoka, A., Muto, T., Momose, M., Tsukagoshi, T., & Dullemond, C. P. 2016, ApJ, 820, 54
Kataoka, A., Tsukagoshi, T., Pohl, A., et al. 2017, ApJL, 844, L5
Konigl, A., & Pudritz, R. E. 2000, in Protostars and Planets IV, ed. V. Mannings, P. Boss, & S. S. Russell (Tucson, AZ: Univ. Arizona Press), 759
Lee, C.-F., Hirano, N., Zhang, Q., et al. 2014, ApJ, 786, 114
Lee, C.-F., Ho, P. T. P., Beuther, H., et al. 2006, ApJ, 639, 292
Lee, C.-F., Ho, P. T. P., Li, Z.-Y., et al. 2017a, NatAs, 1, 0152
Lee, C.-F., Kwon, W., Jhan, K.-S., et al. 2019, ApJ, 879, 101
Lee, C.-F., Li, Z.-Y., Ching, T.-C., et al. 2018a, ApJ, 854, 56
Lee, C.-F., Li, Z.-Y., Codella, C., et al. 2018b, ApJ, 856, 14
Lee, C.-F., Li, Z.-Y., Ho, P. T. P., et al. 2017b, SciA, 3, e1602935
Lee, C.-F., Li, Z.-Y., Ho, P. T. P., et al. 2017c, ApJ, 843, 27
Lee, C.-F., Li, Z.-Y., & Turner, N. J. 2020, NatAs, 4, 142
Lee, C.-F., Tabone, B., Cabrit, S., et al. 2021, ApJL, 907, L41
Lee, H. M., & Draine, B. T. 1985, ApJ, 290, 211
Lin, Z.-Y. D., Lee, C.-F., Li, Z.-Y., et al. 2021, MNRAS, 501, 1316
Lin, Z.-Y. D., Li, Z.-Y., Yang, H., et al. 2020, MNRAS, 493, 4868
Liu, H. B. 2020, arXiv:2010.05392
Ohashi, S., Kataoka, A., Nagai, H., et al. 2018, ApJ, 864, 81
Padoan, P., Goodman, A., Draine, B. T., et al. 2001, ApJ, 559, 1005
Reissl, S., Wolf, S., & Brauer, R. 2016, A&A, 593, A87
Sadavoy, S. I., Myers, P. C., Stephens, I. W., et al. 2018a, ApJ, 859, 165
Sadavoy, S. I., Myers, P. C., Stephens, I. W., et al. 2018b, ApJ, 869, 115
Shakura, N. I., & Sunyaev, R. A. 1973, A&A, 500, 33
Stephens, I. W., Yang, H., Li, Z.-Y., et al. 2017, ApJ, 851, 55
Tabone, B., Cabrit, S., Bianchi, E., et al. 2017, A&A, 607, L6
Tabone, B., Cabrit, S., Pineau des Forêts, G., et al. 2020, A&A, 640, A82
Tobin, J. J., Sheehan, P. D., Megeath, S. T., et al. 2020, ApJ, 890, 130
Wiseman, J., Wootten, A., Zinnecker, H., & McCaughrean, M. 2001, ApJL, 550, L87
Wood, K. 1997, ApJL, 477, L25
Yang, H., Li, Z.-Y., Looney, L., & Stephens, I. 2016a, MNRAS, 456, 2794
Yang, H., Li, Z.-Y., Looney, L. W., et al. 2016b, MNRAS, 460, 4109
Yang, H., Li, Z.-Y., Looney, L. W., Girart, J. M., & Stephens, I. W. 2017, MNRAS, 472, 373
Yen, H.-W., Koch, P. M., Hull, C. L. H., et al. 2021, ApJ, 907, 33
Zinnecker, H., McCaughrean, M. J., & Rayner, J. T. 1998, Natur, 394, 862